nature communications

Article

https://doi.org/10.1038/s41467-024-55445-x

A stable and biocompatible shortwave infrared nanoribbon for dual-channel in vivo imaging

Received: 26 June 2024

Accepted: 11 December 2024

Published online: 02 January 2025

Check for updates

Cheng Yao[1,2], Ruwei Wei[1,2], Xiao Luo[3], Jie Zhou[4,5], Xiaodong Zhang[1,2], Xicun Lu[1,2], Yan Dong[1,2], Ruofan Chu[1,2], Yuxin Sun[1,2], Yu Wang[3], Wencheng Xia[6], Dahui Qu[1], Cong Liu[6], Jun Ren[7], Guangbo Ge[8], Jinquan Chen[4,5], Xuhong Qian[1,2,3] & Youjun Yang[1,2]

The shortwave infrared (SWIR) region is an ideal spectral window for next-generation bioimaging to harness improved penetration and reduced phototoxicity. SWIR spectral activity may also be accessed via supramolecular dye aggregation. Unfortunately, development of dye aggregation remains challenging. We propose a crystal-aided aggregate synthesis (CAASH) approach to introduce a layer of rationality for the development of J-aggregate and the successful development of a water-soluble SWIR JV-aggregate with a bisbenzannulated silicon rhodamine scaffold (ESi5). The resulting SWIR-aggregates exhibit excellent stabilities toward organic solvents, pH, sonication, photobleaching, thiols, and endogenous oxidative species. Notably, the aggregates have a high structure-dependent melting temperature of *ca*. 330-335 K. In fact, the heating/annealing process can be exploited to reduce aggregation disorder. The aggregates are biocompatible and have broad potential in in vivo fluorescence and photoacoustic imaging and more.

Shortwave infrared (SWIR), i.e., 1000 nm and beyond, is an ideal spectral window for deep-tissue and high-contrast in vivo imaging, disease diagnosis, phototherapies, and surgery navigation[1–4]. SWIR-active materials of diverse nature have been reported and found applications, e.g., inorganic low-bandgap materials in infrared optoelectronics[5–7] and electrochromic smart windows[8], hybrid materials in optical filtering and laser shielding[9], and organic dyes in infrared photography[10], lasing[11], and OLED[12]. Yet, all these existing SWIR materials have limitations to overcome to improve their potential in the aforementioned cutting-edge biomedical applications. Inorganic or hybrid SWIR materials contain heavy transition metals, the long-term toxicity of many of which are still to be systematically evaluated[13]. Though organic dyes typically exhibit good biocompatibility, SWIR-absorbing organic dyes have their own challenges[13,14]. Imparted by their high-lying HOMO and low-lying LUMO, SWIR dyes inevitably suffer from poor stabilities, which inhibit their practical and clinical applications. First, their conjugative backbones are readily destructed, either irreversibly by endogenous/photo-induced oxidative species[15,16],

[1]State Key Laboratory of Bioreactor Engineering, East China University of Science and Technology, Shanghai, China. [2]Shanghai Key Laboratory of Chemical Biology, Shanghai Frontiers Science Center of Optogenetic Techniques for Cell Metabolism, School of Pharmacy, East China University of Science and Technology, Shanghai, China. [3]Shanghai Engineering Research Center of Molecular Therapeutics and New Drug Development, School of Chemistry and Molecular Engineering, East China Normal University, Shanghai, China. [4]State Key Laboratory of Precision Spectroscopy, East China Normal University, Shanghai, China. [5]School of Physics and Electronic Science, East China Normal University, Shanghai, China. [6]Interdisciplinary Research Center on Biology and Chemistry, Shanghai Institute of Organic Chemistry, Chinese Academy of Sciences, Shanghai, China. [7]Hubei Key Laboratory for Precision Synthesis of Small Molecule Pharmaceuticals & Ministry of Education Key Laboratory for the Synthesis and Application of Organic Functional Molecules, Hubei University, Wuhan, China. [8]Institute of Interdisciplinary Integrative Medicine Research, Shanghai University of Traditional Chinese Medicine, Shanghai, China. e-mail: youjunyang@ecust.edu.cn

or reversibly by ubiquitous nucleophiles[17]. Second, the electron-delocalization along the long conjugative backbone accounting for their SWIR spectral activity is readily disrupted by water via dipole-induced Peierls transition[18]. Concomitantly, their long-wavelength absorption band becomes weak, broad, and often significantly blue-shifted[19]. Rendering thermodynamically unstable SWIR dyes kinetically persistent in the biological milieu is the key to circumventing their instabilities. An obvious and convenient approach is supramolecular encapsulation in polymer[20], serum albumin[21], or porous materials[22]. Molecular steric shielding approaches have also been developed for squaraines[23,24], cyanines[25,26], and polybenzannulated xanthenoids[27–29]. Generally speaking, this approach becomes exponentially difficult when the absorption maximum marches deeper into the SWIR and their conjugative scaffold concomitantly becomes larger. Alternative robust strategies to develop stable and biocompatible SWIR-absorbing/emitting materials are a timely addition to the field.

The rationalization of aggregation-induced bathochromism led to the formulation of the exciton theory[30], the mechanistic elucidation of the natural wonder of photosynthesis[31], and the later emergence of the nowadays prosperous field of dye aggregation[32–34]. The highlight of this strategy for SWIR-active materials is that the resulting longer-wavelength J-aggregate can enjoy the higher stability of the shorter-wavelength monomer. Harnessing the power of J-aggregation for SWIR spectral activity is eminently promising, and yet remains an endeavor necessitating both rationality and serendipity[33]. An elusive but useful guideline has been empirically established in designing suitable monomeric dyes for J-aggregation. The monomeric dye ideally exhibits a large transition dipole moment to enhance dipole coupling[35]. Its electron push–pull headgroups should be flat to allow stacking. A molecular twist or a bulky group should exist at the center of its conjugative backbone to inhibit the undesired co-facial H-type aggregation[32,36]. Beyond these electronic and structural nuances, dyes should self-assemble or be organized in a topologically and orientationally precise fashion. Mother Nature has mastered both approaches and crafted astoundingly elaborate functional complexes such as photosynthetic machineries[31]. The nature's prowess in protein engineering is beyond our scope of synthetic access. Matrices like DNA[37], polymer[38], mesoporous silica[39], hydrogel[40], and liposome[41], have also been explored to template the aggregate synthesis. Besides, a number of environmental parameters, e.g., counterions, solvent, pH, temperature, and ionic strengths, can also be tinkered with to influence the aggregation outcome[42–46]. The implementation of this guideline has led to a number of elegant J-type aggregates based on, e.g., porphyrin(oid)s[47,48], PDI[49,50], BODIPY/aza-BODIPY[51,52], squaraine[53,54], and Cyanine[55,56]. Unfortunately, the vast majority of these J-type aggregates typically exhibit an absorption maximum well within 1000 nm[55,57]. Aggregates with a SWIR-absorption maximum are few and exhibit a rather broad absorption and a Stokes-shifted emission, suggesting disorder in aggregation due to the high structural flexibility of the corresponding NIR monomeric dyes[43,58–60]. Additionally, most SWIR aggregates are synthesized in organic solvents and lack biocompatibility. Also, some J-aggregates, e.g., double-walled nano-tube, are not thermodynamically stable and may exhibit polymorphism[61–63]. We recently reported a bisbenzannulated silicon-rhodamine (ESi5) dye[28]. The ESi5 scaffold has flat electron-donating headgroups, bulky groups at the center, a rigid conjugative scaffold, and a deep-NIR absorption maximum at 867 nm, the combination of which structural and electronic properties promote us to develop high-performance J-aggregate for in vivo bioimaging applications starting from this ESi5 scaffold.

Herein, we report a stable and biocompatible SWIR aggregate via crystal-aided aggregate synthesis (CAASH). It is a two-layer nanoribbon exhibiting a V-type intra-chain packing and a J-type inter-chain packing. The spectral signature of this unusual packing is two red-shifted peaks along with one blue-shifted sharp peak. Notably, the aggregate is stable toward H_2O, pH, sonication, photobleaching, oxidative species, and sulfides. Its aggregation is temperature-dependent and fully reversible. Aggregation disorder could be reduced by repeated heating-annealing. The design and synthesis of robust molecular SWIR aggregate offer a fascinating photophysical playground to formulate/test photophysical principles and high-performance materials for numerous cutting-edge biotechnologies.

Results

Design guideline

Our design of SWIR-absorbing aggregate started with the crystallization of ESi5, a bright cationic fluorophore absorbing at 867 nm. Interestingly, two distinct crystal structures of ESi5 were obtained when different counterions were used. With Cl^-, ESi5 stacks into a conventional brickwork J-aggregated wall, which further aligns with other walls in an H-fashion to form the 3D crystal packing (Fig. 1a). Following the literature convention, such a packing was referred to as an HJ-aggregate[64]. With PF_6^-, ESi5 adopts a different zig-zag intra-chain packing mode with a 121.1° angle between two proximal dyes (Fig. 1b). Such an oblique-dimer was pictorially referred to as a V-dimer[65,66]. When two such walls are brought together in a co-facial fashion, their inter-chain packing mode is no longer H-type, but J-type with a slipping angle of 51.7°. For this reason, this aggregate is referred to as JV-aggregate. Suppose we can trim off the crystal layer by layer until the last two layers, which stack to each other via π–π interaction. To further render such two-layer stack stability and biocompatibility in aqueous medium, two flexible hydrophilic chains can be installed at the electron push–pull headgroups of the dye. Following this idea, we displaced the two chlorine atoms of the ESi5 with azido groups, and further clicked it to a terminal alkyne linked to various water-soluble groups (Fig. 1c). Such judiciously functionalized amphiphilic ESi5 is expected to spontaneously aggregate in an aqueous medium. However, the specific aggregation outcome, e.g., HJ-type, JV-type, or any other unexpected fashion, is serendipitous, but can be deduced by correlating their absorption spectral features with their packing style in the crystal structure. As for ESi5, a single red (or blue)-shifted peak would suggest a J- (or H-) aggregate, while a V-aggregate would result in a red-shifted peak along with a blue-shifted peak via energy-splitting. The relative intensities of the two peaks depend on the angle in between. Suppose the angle (α) remains at *ca.* 120°, the oscillation strengths of the J-band (f_J) are expected to be roughly three times that of the H-band (f_H), according to $f_J/f_H = tg^2(\alpha/2)$[67].

Photophysical properties

The fluorochromic core of ESi5 is cationic, and installation of anionic terminal results in amphiphilicity, imparting a driving force to aggregate in an aqueous medium. We prepared eight ESi5 derivatives with different water-soluble groups, i.e., **ESi5-NS** with a zwitterion, **ESi5-N** with a quaternary ammonium, **ESi5-S** with a sulfonate, **ESi5-C1**(**-C5**) with a carboxylate-caped linear alkyl chain of 1–5 carbon atoms (Fig. 2a). The surface electrostatic potential of each was mapped to qualitatively assess their potential to aggregate (Fig. 2b). An aliquot of each compound (5 mM, 2 μL) in MeOH was added to H_2O (2 mL) with stirring, and their UV-Vis absorption spectra were then acquired without further sitting. No spectral feature of aggregate formation was observed for **ESi5-NS** and **ESi5-N**. The gradual addition of NaCl (200 mM) to the solution containing **ESi5-NS** resulted in a spectral blue shift from 867 nm of **ESi5** dye to 744 nm, suggesting the formation of an undesirable H-type aggregate (Table 1). This H-aggregate of **ESi5-NS** was non-fluorescent. **ESi5-N** did not aggregate even in the presence of NaCl (200 mM), likely due to its tri-cationic feature (Fig. 2c). In sharp contrast, the **ESi5-S** and **ESi5-C1**(**-C5**) aggregated instantaneously upon the addition its MeOH stock into H_2O (Supplementary Fig. 15). Their resulting absorption spectra exhibited similar spectral features, i.e., a lower-intensity red-shifted peak at 1098 nm, another red-shifted peak

https://doi.org/10.1038/s41467-024-55445-x

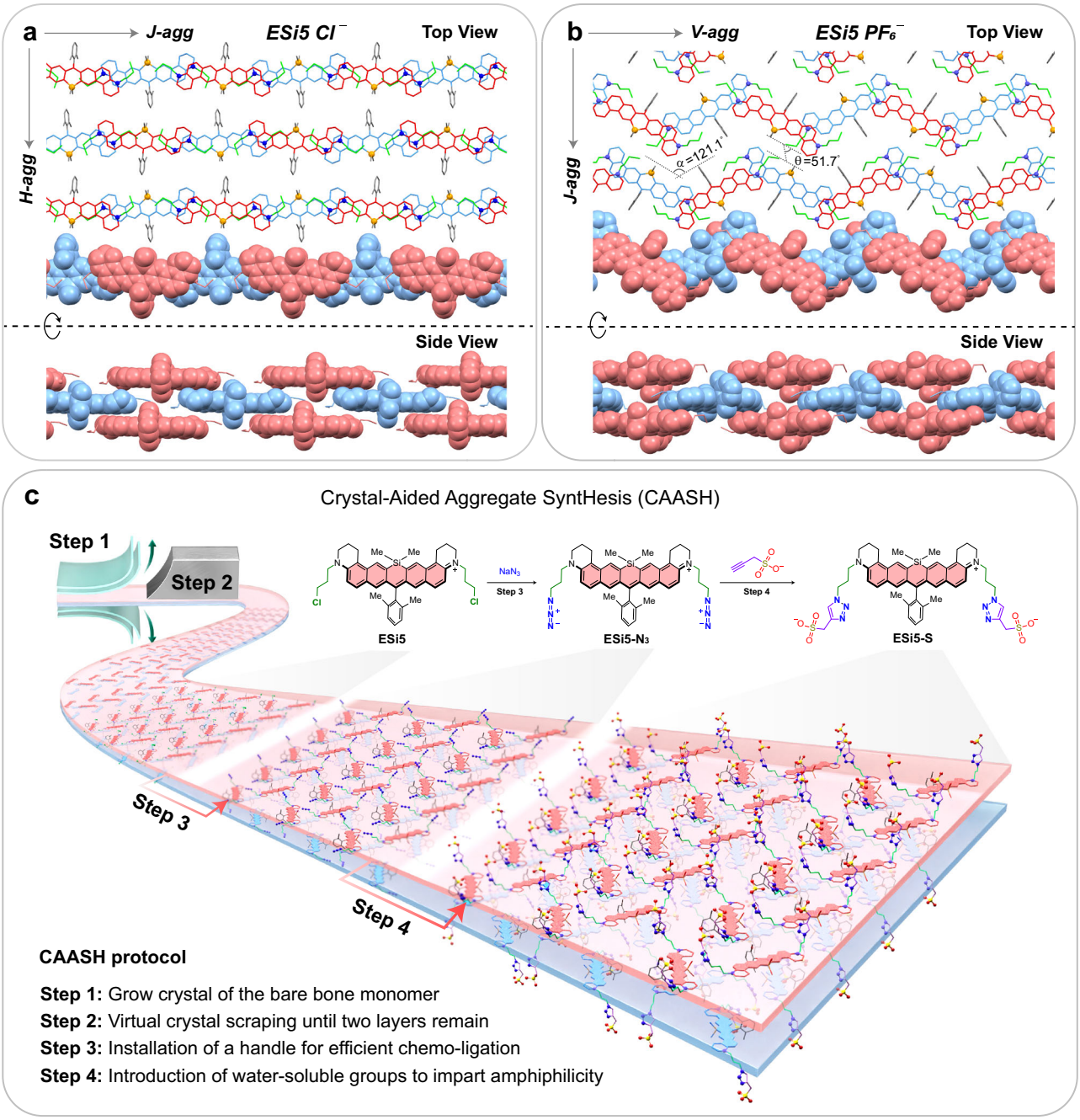

Fig. 1 | The molecular packing of ESi5 in single crystals and the design of its JV-aggregates. The top view and side view of the packing mode of **ESi5•Cl**$^-$ (**a**) and **ESi5•PF$_6$**$^-$ (**b**). **c** The crystal-aided aggregate synthesis (CAASH) with the ESi5 dye.

at 1038 nm of much higher intensity, a blue-shifted peak at 696 nm of comparable intensity to the peak at 1098 nm, and non-resolved vibronic bands between 696 nm and 1038 nm (Table 1).

The unambiguous resolution of the packing mode of an aggregate remains a grand challenge for the field. An advantage of the CAASH approach is that the crystal structure of the monomeric dye provides a reliable source of reference. Such a three-peak pattern cannot possibly be the result of an HJ-type packing in Fig. 1a, but is in agreement with the JV-type packing in Fig. 1b. The two bands at 1038 and 696 nm are presumably due to the intra-chain V-aggregation of **ESi5**, based on the fact that their oscillation strengths are in a *ca.* 3:1 ratio (vide ante) (Table 1). The remaining reddest peak at 1098 nm has to be the result of an inter-chain two-dimensional J-aggregation. The peak width is an indicator of the dipolar coupling strength and calculated via spectral deconvolution. The FWHM of all three peaks are small at 574.0 cm^{-1} for 696 nm, 452.6 cm^{-1} for 1038 nm, and 233.3 cm^{-1} for 1098 nm, respectively, suggesting a strong dipolar coupling between proximal ESi5 dyes. Upon photoexcitation at 696 nm, 1038 nm, or 1098 nm of a solution of **ESi5-S agg** or **ESi5-C1**(**-C5**) **agg**, the same resonant fluorescence emission band at *ca.* 1106 nm was observed with a very sharp FWHM of 481.9 cm^{-1} (Table 1). The fluorescence quantum yield was 0.06% for **ESi5-S**, significantly reduced compared to 1.7% of the monomer. Through a transient absorption study, a fluorescence lifetime of 58 ps was calculated (Supplementary Fig. 31). The change of the terminal anion from sulfonate to carboxylate slightly led to a reduced degree of spectral resolution between the two red-shifted peaks, and enhanced minor vibronic peaks between 1038 and 696 nm. Increasing the length of the alkyl chain from the -CH_2- of **ESi5-C1** to the -$(CH_2)_5$- of

https://doi.org/10.1038/s41467-024-55445-x

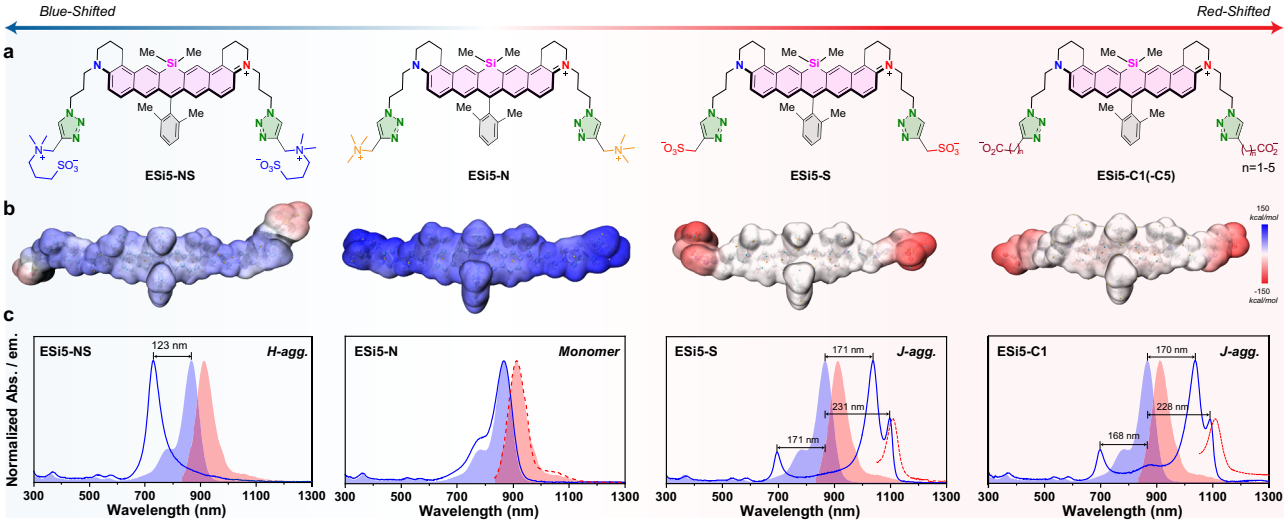

Fig. 2 | The spectral monitoring of the aggregation of ESi5 dyes with different water-soluble groups. a The chemical structures of **ESi5-NS**, **ESi5-N**, **ESi5-S**, and **ESi5-C1**(**-C5**). **b** The electrostatic potential surfaces calculated for **ESi5-NS**, **ESi5-N**, **ESi5-S** and **ESi5-C1** at B3LYP/6-31G level. **c** The UV-Vis absorption (Blue, solid line) and the fluorescence emission (Red, dash line) spectra of the resulting solution upon dilution of the MeOH stock of **ESi5-NS**, **ESi5-N**, **ESi5-S**, and **ESi5-C1** in PBS (pH = 7.4, 10 mM). The UV-Vis absorption (Blue, space-filled) and emission spectra (Red, space-filled) of **ESi5** in MeOH were plotted for comparison purposes.

Table 1 | The photophysical properties of ESi5 in MeOH and ESi5-NS, ESi5-N, ESi5-S, and ESi5-C1(-C5) in PBS (pH = 7.4, 10 mM)

The photophysical properties									
	Monomer	**ESi5-NS**	**ESi5-N**	**ESi5-S**	**ESi5-C1**	**ESi5-C2**	**ESi5-C3**	**ESi5-C4**	**ESi5-C5**
λ_{abs} (nm)	867	744	866	1038	1037	1024	1022	1033	1019
λ_{abs} (nm)	–	–	–	1098	1095	1082	1080	1080	1075
λ_{abs} (nm)	–	–	–	696	699	700	708	701	709
λ_{em} (nm)	909	–	911	1106	1108	1090	1100	1097	1101
Stokes Shift (nm)	43	–	45	8	13	8	20	17	26
ε (×10^5 cm^{-1} M^{-1})	1.95	–	1.74	0.88	0.79	0.81	0.82	0.86	0.78
ϕ (%)	16	–	1.6	0.06	0.04	0.02	0.02	0.02	0.02
(ε × ϕ) (cm^{-1} M^{-1})	15,054	N/A	2784	52.8	31.6	16.2	16.4	17.2	15.6

The **ESi5-NS** solution contains NaCl (2 M) in PBS.

ESi5-C5 resulted in a slight broadening of the absorption bands (Supplementary Figs. 16–21).

Morphology of ESi5 aggregates

The morphology of the **ESi5-S agg** was different with respect to the sitting time of the solution. Without sitting time, the aggregate adopted the form of small particulate with a diameter of 7.7 ± 0.6 nm (Supplementary Fig. 29A). In 6 h, the particulate could still be seen while the aggregate predominantly existed in form of short nanoribbon with an average width of 39.6 ± 1.6 nm, and an average length of 0.44 μm (Supplementary Fig. 29B). In 24 h, the short nanoribbon further grew into a network. Some ribbons exhibited an increased width of up to 116.2 ± 2.2 nm (Fig. 3a, Supplementary Fig. 29C). Some ribbons folded back and forth suggesting a soft and flexible nature. The nanoribbon morphology of **ESi5-S agg** in solution was clearly captured by the cryo-electron microscopy (cryo-EM) image (Fig. 3b). The thickness of the ribbon was determined to be *ca.* 3.4 nm by atomic force microscopy (AFM), in agreement with the hypothesized double-layer aggregate model (Fig. 3c, d). The transmission electron microscopy (TEM) images of **ESi5-C1/C2/C3 agg** revealed that their morphologies were similar to that of **ESi5-S agg** (Supplementary Figs. 24–28). As for **ESi5-C4/C5 agg**, the ribbon was significantly shorter and wider. The existence of particulate in the TEM images of **ESi5-C4/C5 agg** suggested that their aggregation displayed inhomogeneity, likely due to the enhanced structural flexibility of the monomer dye (Supplementary Figs. 27 and 28). The thickness of aggregates increased with respect to the chain length from 3.4 nm of **ESi5-C1 agg** to 5.8 nm of **ESi5-C5 agg** (Supplementary Figs. 24–28). Despite the morphological change, it was interesting to note that the absorption spectra of the bulk aggregate solution remained unchanged. This indicated that the molecular packing of the monomer in the particulate at 0 h, short nanoribbon at 6 h, and long nanoribbon network at 24 h remained unchanged.

Governing parameters on aggregation

With **ESi5-S agg** as an example, the stabilities of the JV-aggregates of ESi5 dyes toward organic solvent, dye concentration, sonication, pH, temperature, light irradiation, and oxidants were thoroughly evaluated. The UV-Vis absorption spectra of **ESi5-S agg** (5 μM) in a mixture of neutral PBS buffer and varying percentages of MeOH (0%–32%, v/v) were acquired (Fig. 4a, b). The absorption spectrum remained essentially unchanged when the MeOH percentage was below 6%. When the MeOH percentage went above 6%, the peaks of the JV-aggregate started to decrease, and the peak of the monomer at 867 nm started to increase accordingly. When the MeOH percentage was 22%, a 50% aggregation was observed. Raising the MeOH beyond 32% eventually

https://doi.org/10.1038/s41467-024-55445-x

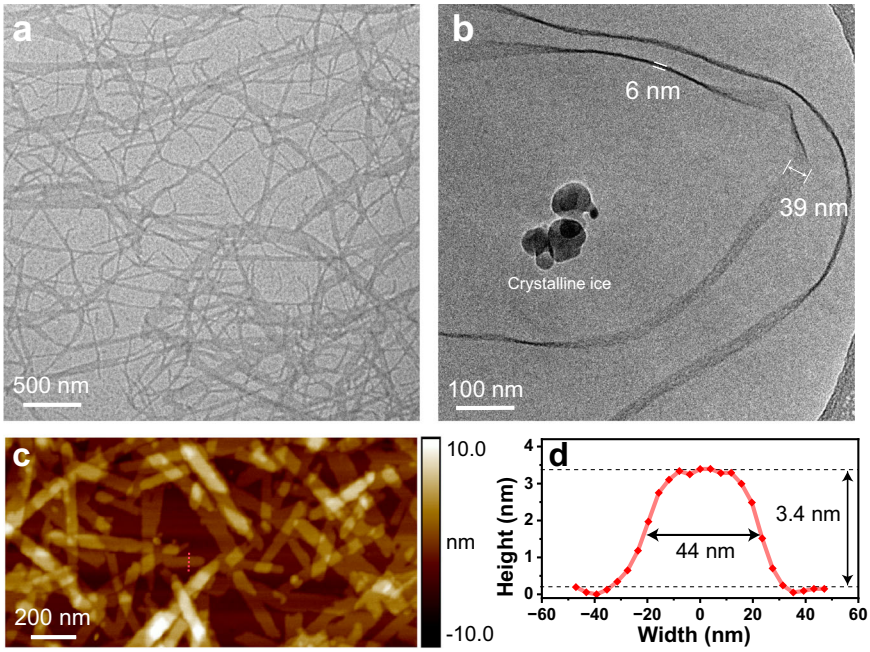

Fig. 3 | Morphology of ESi5-S agg**.** The TEM image (**a**) and the Cryo-EM image (**b**) of **ESi5-S agg** (200 μM) in H_2O. **c** The AFM image of **ESi5-S agg** with cross-section analyses (**d**) along red dashed lines. The dark spots are crystalline ice. Each experiment was repeated independently with similar results ($n = 3$).

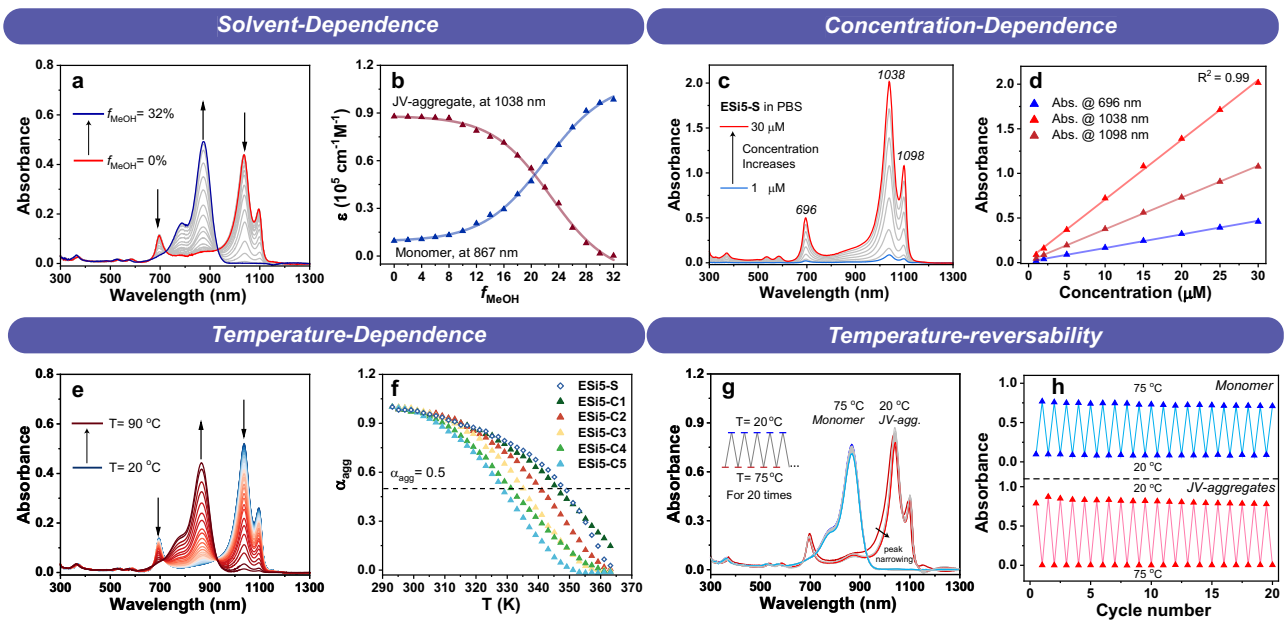

Fig. 4 | The stabilities of JV-aggregate toward different stimuli. a Solvent-dependent changes of the absorption spectra of **ESi5-S** (5 μM) in PBS (pH = 7.4, 10 mM) with different MeOH fractions (f_{MeOH}) from 0% to 32% at room temperature. **b** The plot of molar absorptivities of **ESi5-S** monomer (867 nm) and JV-aggregate (1038 nm) with respect to the f_{MeOH}. **c** The concentration-dependent absorption spectra of **ESi5-S** in PBS (pH = 7.4, 10 mM, containing <2% MeOH) at room temperature from 1 to 30 μM. **d** The plot of absorbance at 696, 1038, and 1098 nm, respectively, as a function of the concentration of **ESi5-S**. **e** The temperature-dependent absorption spectra of **ESi5-S agg** (5 μM) in PBS (PH = 7.4, 10 mM) with 5% MeOH from 20 to 90 °C. **f** The plot of aggregation percentage (α_{agg}) with respect to the temperature. **g** The absorption spectra of **ESi5-S** (10 μM) in PBS (pH = 7.4, 10 mM) with 10% MeOH upon repeated heating/annealing between 20 and 75 °C. **h** The reversible absorbance changes of the monomer at 867 nm and the **ESi5-S agg** at 1038 nm with respect to heating and annealing cycles.

totally inhibited the formation of JV-aggregate. **ESi5-S** exhibited a high tendency to aggregate. In the literature, a high dye concentration of 10^{-4}–10^{-3} M^{-1} was routinely used to promote aggregation. Yet, **ESi5-S** at even 1 μM is completely aggregated. Further increasing the dye concentration gave a linear increase in the absorbance at 696, 1038, and 1098 nm with respect to the dye concentration, tested up to 30 μM (Fig. 4c, d). This experiment could help to determine the ideal concentration for bioimaging.

The temperature dependence of the aggregation was studied with a solution of **ESi5-S** (5 μM) in PBS with 5% MeOH. When the temperature gradually raised from room temperature to 90 °C, the aggregation degree (α_{agg}) decreased from near unity at 25 °C, to *ca.* 2.8% at 90 °C

Table 2 | The thermodynamic parameters of ESi5-S, and ESi5-C1(-C5) aggregation

The thermodynamic parameters						
	T_m (K)	K_e (10^5 M^{-1})	DP_N	ΔH (kJ mol^{-1})	ΔS (kJ mol^{-1})	ΔG (kJ mol^{-1})
ESi5-S	349	8.2	2.59	−74.8	118.3	−36.6
ESi5-C1	345	7.1	2.45	−79.9	135.3	−36.2
ESi5-C2	341	6.3	2.31	−86.7	157.6	−35.8
ESi5-C3	335	4.1	2.02	−96.3	190.6	−34.7
ESi5-C4	331	2.9	1.80	−100.3	206.0	−33.8
ESi5-C5	328	2.2	1.66	−111.9	243.9	−33.1

(Fig. 4e). Its melting temperature (Tm, when $\alpha_{agg} = 50\%$), was 74 °C (Fig. 4f, Table 2). When the solution temperature was further lowered back to 25 °C from 90 °C, the absorption of the aggregate was essentially restored. Interestingly, the absorption band at 1038 nm and the 1098 nm became narrower, and their separation became slightly wider. Likely, the heating/annealing process eliminated some of the aggregation defects and further enhanced dipolar coupling. We then repeated the heating/annealing processes over 20 times, and the system showed excellent reversibility (Fig. 4g, h). This experiment not only highlighted the stability of the aggregate, but also was a manifestation of the high stability of the monomeric ESi5 dyes at demanding conditions, i.e., 75 °C in PBS for hours. The aggregate equilibrium constant (K_e) and Gibbs free energy (ΔG) of **ESi5-S** aggregate were calculated to be 8.2×10^5 M^{-1}, and −36.6 kJ•M^{-1}, respectively. Changing the sulfonate of **ESi5-S** into the carboxylate of **ESi5-C1** led to a slight decrease of T_m to 69 °C, K_e to 7.1×10^5 M^{-1}, and ΔG to −36.2 kJ•M^{-1} (Table 2). Further elongation of the alkyl chain led to a notable further decrease of the aggregate stability (Table 2, Supplementary Fig. 36). The heating-annealing results with **ESi5-S agg** promoted us to wonder if the same method could be applied to the **ESi5-C1**(**-C5**) since their aggregation disorder seemed to be more pronounced than **ESi5-S**. The solutions of **ESi5-C1**(**-C5**) aggregates in PBS with 5% MeOH were heated to 90 °C and then cooled to room temperature (Supplementary Fig. 15). The effect was very obvious. Three major bands at *ca.* 1098 nm, *ca.* 1038 nm, and *ca.* 696 nm became sharper in shape. The two spectrally unresolved red bands were now totally resolved. The two red bands slightly red-shifted by *ca.* 8 nm, and the blue band slightly blue-shifted by *ca.* 12 nm. These were indications of the reduction of aggregate disorder. **ESi5-S agg** was also stable toward sonication and pH change (Supplementary Figs. 34 and 35).

SWIR-absorbing dyes are usually very susceptible to nucleophilic attack of $ONOO^-$. Yet, the stability of the JV-aggregate of **ESi5-S** and **ESi5-C1**(**-C5**) was all very high. The addition of up to $ONOO^-$ (50 μM, *ca.* 100-fold of the maximum physiological concentration) into its solution resulted in only 10.5% decrease of the aggregate absorbance. Addition of H_2O_2 (5 mM), GSH (60 mM), cysteine (5 mM), and HS^- (tested to 1 mM) did not induce absorbance decrease (Supplementary Fig. 33). Also, the aggregate and monomer exhibited high photostability and irradiation of the solution at 808 nm or 1064 nm for 30 min resulted in an absorbance decrease of only *ca.* 4.8% and 11.8%, respectively, while the absorbances of ICG at 808 nm irradiation and **IR1064** at 1064 nm irradiation decreased by 98.7% and 85.9%, respectively (Supplementary Fig. 32).

In vivo fluorescence imaging

ESi5-S agg exhibited good biocompatibility. **ESi5-S agg** was essentially non-cytotoxic when its concentration was smaller than 30 μM, since the cells viability was higher than 85% after a 24 h incubation with HeLa cells (Supplementary Fig. 38). Incubating **ESi5-S agg** (100 μM) with red blood cells for 24 h did not induce noticeable hemolysis (<5%) (Supplementary Fig. 39). An acute-toxicity study was carried out to verify that up to 2.5 mg/kg did not exhibit toxicity based on monitoring of the weight and post-mortal H&E histological analysis (Supplementary Figs. 45 and 46). We further tested the feasibility of **ESi5-S agg** for in vivo fluorescence imaging harnessing its intense and narrowband SWIR absorption and high stability in an aqueous medium. Upon *i.v.* injection, an aggregate is diluted and re-establishes the aggregation-disaggregation equilibrium in blood vessels. Therefore, a dual-channel imaging experiment may be carried out to monitor the fluorescence of the aggregate ($\lambda_{ex} = 1064$ nm) and that of the dissociated monomer ($\lambda_{ex} = 808$ nm). Since the aggregate and the monomer are drastically different in terms of their size, charge, and morphology, they are expected to exhibit distinct metabolic profiles and in vivo distribution. We further verified that the aggregate can be selectively excited by a 1064 nm laser and the monomer by an 808 nm laser, respectively, with minimal cross-talk (Fig. 5a, b). An aliquot of **ESi5-S agg** solution (500 μM in PBS, 100 μL) was injected into a BALB/c mouse through the tail vein to render a final vasculature concentration of 2.5 mg/kg, equivalent to a biocompatible blood concentration of *ca.* 30 μM. The first set of images was acquired 10 min post injection (Fig. 5e). The fluorescence signal of the aggregate was found from such organs as the liver, spleen, and bones, whereas the signal of the monomer localized in the liver (Fig. 5e–g). The blood vessels were not observed in either channel. This suggests that the aggregate exhibited a notable stability against dissociation even in blood and was distributed through circulation. Its affinity toward bone was likely due to its polyanionic nature. This bone affinity was also in agreement with many other polyanionic materials, due to its affinity to hydroxyapatite[68] (Supplementary Fig. 47). The ratio of the fluorescence intensities between the vertebrae and soft tissue reached a peak of 3.9 in 180 min (Supplementary Fig. 41). Besides, the analysis crossing the vertebrae and shin also showed good differentiation between bone and others, with FWHM of 0.89 mm and 1.80 mm (Fig. 5k, l).

During a course of 180 min, the fluorescence images of these two channels were acquired intermittently. The distribution pattern was essentially unchanged except for a gradual decrease in signal intensity. The fluorescence images of the liver region of the two channels provided a good estimate of the metabolic kinetics of the monomer and the aggregate to be on the order of a few hours (Fig. 5h, i). This suggested a gradual dissociation and metabolism of the aggregate. In 180 min, the monomer was metabolized from the liver to the intestine (Fig. 5f). Line intensity profile could be used to calculate the size of various anatomical structures, e.g., sternum to be *ca.* 0.89 mm (Fig. 5k) and tibia to be *ca.* 1.80 mm (Fig. 5l). Likewise, imaging of the prone state (Fig. 5g) also displayed a high sensitivity and SBR in the normal bones, including the lumbar vertebra, ilium, caudal vertebra, and femur. Specifically, line-intensity analysis (red line) along the lumbar vertebra was extracted and afforded the dimensions of all the vertebrae in the range of 1.12–1.63 mm (Fig. 5m). The lack of the monomer signal in other organs except the liver suggested that the dissociation of aggregate occurred predominantly in the liver. Overall, **ESi5-S agg** is a specifically bone-binding nano-assemblies for visualizing the whole skeletal system in vivo, and its enterohepatic metabolism processes are revealed by dual-channel imaging.

https://doi.org/10.1038/s41467-024-55445-x

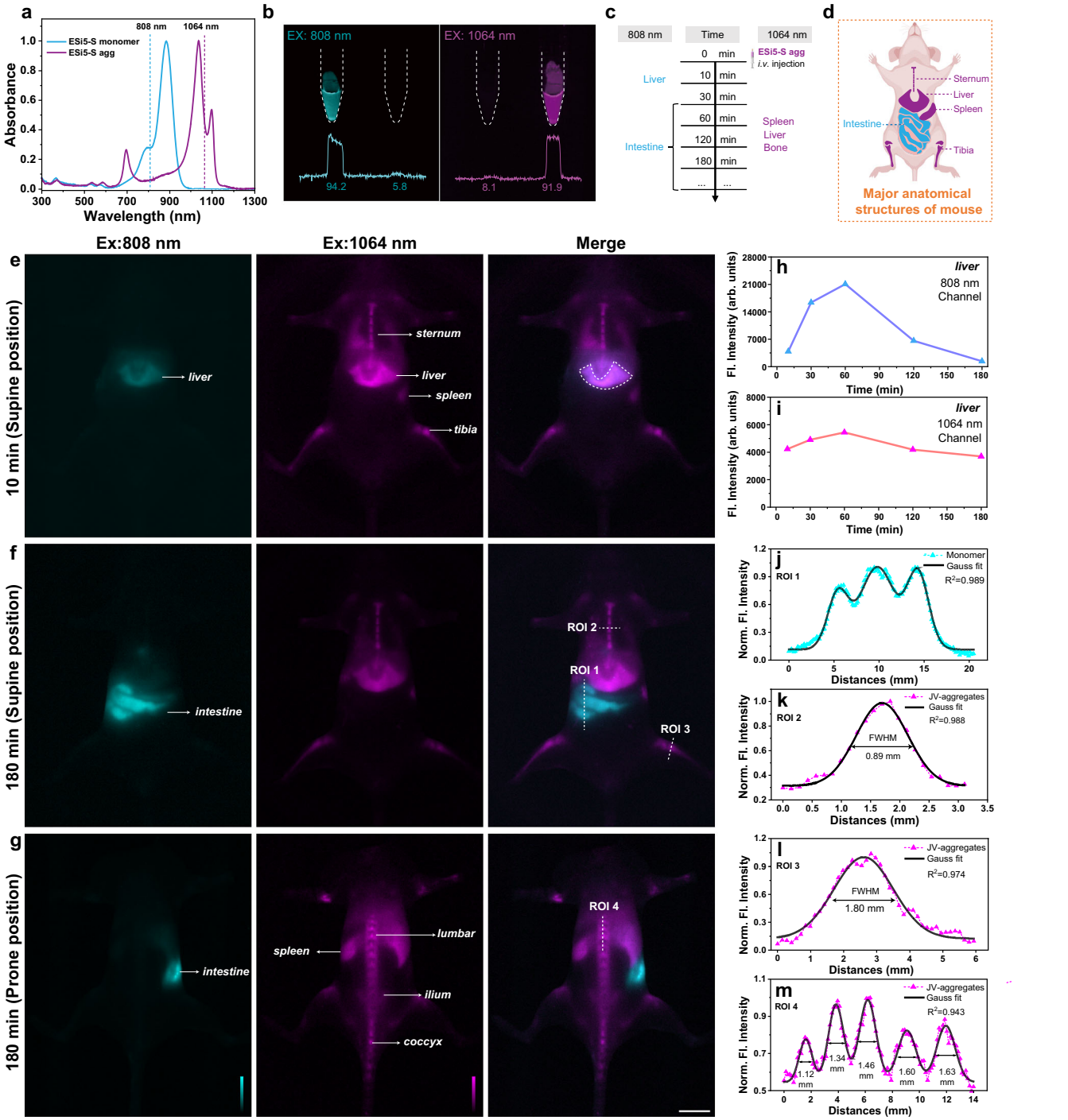

Fig. 5 | The in vivo dual-channel fluorescence (Fl.) imaging of BALB/c mouse using ESi5-S agg**. a** The normalized absorption spectra of **ESi5-S** monomer and **ESi5-S agg** and the compatible common laser lines. **b** The epi-fluorescence images of the **ESi5-S** Monomer (Left, 500 μM in water with 1% tween 80) and **ESi5-S agg** (500 μM in PBS) solutions in EP tubes excited by 808 (60 mW•cm^{-2}) and 1064 nm (80 mW•cm^{-2}), respectively. **c** The timeline of the in vivo fluorescence mouse imaging experiment. 808 nm channel: λ_{ex} = 808 nm (60 mW•cm^{-2}), long pass filter: 1200 nm, exposure time: 100 ms. 1064 nm channel: λ_{ex} = 1064 nm (80 mW•cm^{-2}), long pass filter: 1200 + 1350 nm, exposure time: 500 ms. **d** A schematic diagram of major anatomical structures of mouse related to this experiment. Created in BioRender. Yang, Y. (2024) https://BioRender.com/q64i385. The two-channel fluorescence images of BALB/c mice in the supine position (**e**) 10 min and (**f**) 180 min post *i.v.* injection, and in the prone position (**g**) at 180 min post *i.v.* injection. The changes of the liver region fluorescence intensity (**h**) in the 808 nm channel and (**i**) in the 1064 nm channel. The line intensities of (**j**) the ROI 1 for the intestine in the 808 nm channel, (**k**) the ROI 2 for the sternum in the 1064 nm channel, (**l**) the ROI 3 for the tibia in the 1064 nm channel, and (**m**) the ROI 4 for the lumbar vertebra in the 1064 nm channel. Scale bar: 10 mm.

In vivo photoacoustic imaging

An additional proof-of-concept photoacoustic imaging application was carried out to further showcase the potential of this series of aggregates with **ESi5-S agg** as an example for different modalities of bioimaging. PA signal is mainly related to the photothermal conversion and subsequent thermal-to-acoustic transformation of a light-absorbing material. The temperature increase profiles of the **ESi5-S agg** solution in PBS correlated with both the aggregate concentrations and laser power density (Fig. 6a, b). Fitting of the photothermal conversion profile yielded a photothermal conversion efficiency of 58.1%

https://doi.org/10.1038/s41467-024-55445-x

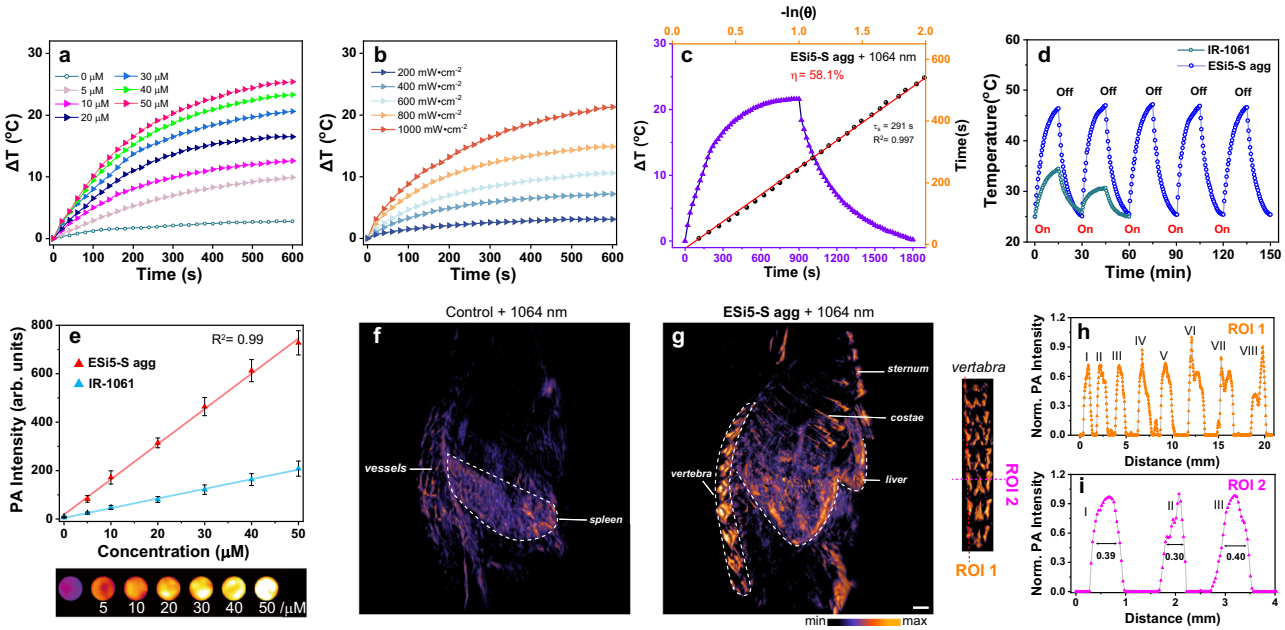

Fig. 6 | The in vivo photoacoustic (PA.) imaging of BALB/c mouse using ESi5-S agg**.** The concentration (**a**) and laser intensity (**b**) dependent photothermal property of **ESi5-S agg** in PBS. **c** The calculation of the photothermal conversion efficiency of **ESi5-S agg** (30 μM) under continuous 1064 nm laser (1000 mW•cm^{-2}) irradiation. **d** Photothermal stability of **ESi5-S agg** (30 μM) in PBS and IR-1061 (30 μM) in PBS under 1064 nm laser (1000 mW•cm^{-2}) irradiation. **e** The photoacoustic intensity of the **ESi5-S agg** and IR-1061 in PBS excited by 1064 nm laser ($n = 3$, Data are presented as mean values ± SD). Photoacoustic imaging of BALB/c mice acquired (**f**) without **ESi5-S agg** and (**g**) 180 min post injection of **ESi5-S agg** (2.5 mg/kg in PBS). **h**, **i** Line intensities of the highlighted ROIs of the images of vertebra. Scale bar: 1 mm.

(Fig. 6c). Further, the thermal stability of the **ESi5-S agg** was evaluated by repeated heating/cooling cycles in the range of 25–46.6 °C (Fig. 6d). After five cycles, no sign of fatigue was observed, while IR-1061 did not survive two around of heating/cooling cycles under the same conditions. The photoacoustic effect of **ESi5-S agg** was further tested at various concentrations (0–50 μM) (Fig. 6e). A dose-dependence was observed between the photoacoustic intensity and the **ESi5-S agg** concentration. Notably, the photoacoustic signal intensity was 3.5 times higher than that of IR-1061 (50 μM in PBS).

The feasibility of **ESi5-S agg** for in vivo photoacoustic imaging was carried out with BALB/c mouse. First, we acquired the background photoacoustic imaging with mouse without injecting **ESi5-S agg**. The presence of weak signals from the vasculature-rich area/organs was due to a weak absorption of hemoglobin at this SWIR region (Fig. 6f). Then, a solution of **ESi5-S agg** (2.5 mg/kg) in PBS was injected into shaved BALB/c mouse through tail vein. Due to its intense absorption at 1064 nm, a good contrast could be obtained over the signal from the hemoglobin. In 180 min, the photoacoustic experiment was carried out with a 1064 nm excitation and a three-dimensional photoacoustic tomography was reconstructed (Fig. 6g). The photoacoustic signal was concentrated in the liver and the bone (including sternum, costae, and lumbar), in agreement with the fluorescence imaging results. For lumbar, specifically, vertical and horizontal analysis (ROI 1 and ROI 2) along the lumbar vertebra showed eight and three peaks of photoacoustic intensity respectively, and the FWHMs were high enough to discriminate different vertebrae including posterior articular protrusion (Fig. 6h, i). From the above experimental results, it can be concluded that the **ESi5-S** exhibits an excellent PA imaging performance.

Discussion

In conclusion, we proposed an approach, i.e., CAASH, to make J-aggregate development more of a rational and less of a serendipitous endeavor. We chose ESi5 as the monomeric dye to develop SWIR aggregate because it fulfills the basic set of criteria: (1) deep-NIR absorption maximum at 867 nm due to a large transition dipole moment; (2) flat electron push–pull headgroups; (3) bulky groups at the center of the conjugative backbone. Implementation of the CAASH approach to the scaffold of ESi5 was a two-step process. First, the tendency of the ESi5 to form aggregate was evaluated by growing the crystals of the bare bone ESi5 fluorophore. Interestingly, we successfully obtained two distinct crystals of ESi5 when different counter-anions were used. With the success of the first step, we then installed two hydrophilic chains to the electron push–pull headgroups of ESi5 scaffold to impart additional driving force to aggregate in an aqueous medium. Upon addition of the amphiphilic ESi5 dyes, e.g., **ESi5-S**, or **ESi5-C1**(**-C5**), into H_2O, spectral features suggesting the formation of an aggregate were immediately observed. The intense absorption at 867 nm of ESi5 monomer disappeared and three new peaks at 696, 1038, and 1098 nm appeared. Taking into account both the basic exciton theory and the crystal packing styles of ESi5 crystal, it was deduced that the 696 and 1038 nm bands were presumably from intra-chain V-aggregation, and the 1098 nm band from inter-chain J-aggregation. Upon photoexcitation, ESi5 aggregates exhibited by a sharp resonant fluorescence emission band and a greatly reduced fluorescence lifetime ($\tau = 58$ ps). The JV-aggregate from ESi5 dyes exhibited unexpectedly high stability toward organic solvent, temperature, photobleaching, and reactive chemical species. Notably, we found that heating/annealing not only did not lead to destruction of the JV-aggregate, but also helped to reduce aggregation disorder and promote aggregation coupling strength. **ESi5-S agg** exhibited high biocompatibility, e.g., high aqueous stability, aqueous solubility, low toxicity, and low hemolysis capability. Together, these properties rendered the ESi5 aggregates broad potential for cutting-edge biotechnologies exploiting the SWIR region. In this work, we intravenously injected an aliquot of **ESi5-S agg** to BALB/c mouse. The **ESi5-S agg** exhibited good stability in the bloodstream and can be used for dual-channel fluorescence bioimaging. The 1064 nm laser line can be used to excite **ESi5-S agg**, which exhibits high affinities toward bones, along with some uptake in the liver and spleen. The 808 nm laser line can be used to excite the monomeric **ESi5-S** dye, which was found only

to exist in the liver and metabolized to the intestine in the course of a few hours. **ESi5-S agg** also enabled photoacoustic tomography of mouse bones, including sternum, costae, and vertebra. Multiplexed imaging with minimal cross-talks between different channels is a challenge for the near-infrared region due to the broad absorption bands of the NIR dyes. Sletten et al. noted that the aggregates with sharp absorption bands are viable candidates for multiplexing in this spectral region[39]. Therefore, developing aggregates that can pair with **ESi5-S agg** for multiplexed imaging is a viable direction for future research.

Methods

Animals

The animal experiment protocol was approved by the Laboratory Animal Welfare and Ethics Committee of Shanghai University of Traditional Chinese Medicine (PZSHUTCM220613018, June 13, 2022). The mice which purchased from Shanghai JieSiJie Laboratory. Six to eight-week-old female BALB/c mice with a body weight of ~20 g were chosen for research. The mice were housed in an environment with a temperature of ~25 °C and a 12 h light/dark cycle, suitable humidity (typically 40%–60%). Sex was not noted in the mouse imaging studies because the results are applicable to both male and female mice.

General materials

Chemicals were purchased from major venders based in China and used without further purification. Analytical grade solvents, including petroleum ether, ethyl acetate, dichloromethane, methanol, dimethyl sulfoxide (DMSO), and *N,N*-dimethylformamide (DMF), were obtained from Titan Scientific. IR-1061 (CAS: 155614-01-0) and ICG (CAS: 3599-32-4) was purchased from Sigma Aldrich. Anhydrous solvents for reactions (e.g. tetrahydrofuran and DMF) were procured from Adamas with activated 4A molecular sieves. Silica gel (200–300 or 300–400 mesh) for flash chromatography was acquired from Haiyang Chem, China. The HeLa cells were purchased from the Cell Bank of Type Culture Collection of the Chinese Academy of Sciences. Sheep red blood cells were purchased from SenBeiJia Biological Technology Co., Ltd.

Instruments

The ^{1}H-NMR and ^{13}C-NMR spectra were acquired over Bruker Avance 400 or Avance 600 spectrometers. The ESI-HRMS spectra were obtained using Micromass GCT spectrometer at the Analysis and Testing Center of East China University of Science and Technology.

The UV-Vis absorption spectra were acquired using a SHIMADZU UV-2600 UV-VIS spectrophotometer and the fluorescence spectra were acquired with a PTI-QM4 steady-state fluorimeter with 1 cm cuvette and an InGaAs photodetector. The femtosecond transient absorption spectra were acquired with Helios fire, ultrafast systems. The single-crystal X-ray diffraction data were acquired with a Rigaku Synergy-R X-ray single-crystal diffractometer. The in vivo fluorescence imaging was carried out with MARS (Artemis Intelligent Imaging) equipped with an InGaAs camera (NIRvana, Teledyne Princeton Instruments). The photoacoustic imaging of solutions and in vivo photoacoustic imaging of mice were performed with the LOIS 3D imaging system (TomoWave Laboratories, USA).

The ^{1}H-NMR and ^{13}C-NMR spectra were processed using MestReNova. The spectral data were processed using Origin 2024b. The microscopy images were analyzed with Image J 1.48. The X-ray crystal diffraction data (cif file) were analyzed using Mercury 3.8, CCDC.

Electrostatic potential (ESP) calculations

All theoretical calculations were accomplished by Gaussian 16. The structural optimization and ESP distribution were derived from density-functional theory calculations at the B3LYP/6-31G (d) level. And the surface density minima or maxima analysis was performed using Multiwfn (*Comput. Chem.* 2012, **33**, 580–592).

Preparation of ESi5 aggregates

Take **ESi5-S** for example, a stock solution of **ESi5-S** (5.0 mM) was prepared in organic solvents, e.g., MeOH, and an aliquot was subsequently added to a PBS (pH = 7.4, 10 mM) solution with stirring. The aggregation was completed essentially instantaneously.

Fluorescence quantum yield (ϕ) determination

The fluorescence quantum yield of ESi5 dyes in organic solvent (i.e. DMSO, MeOH, MeCN, DMF) and **ESi5-N** in PBS were referenced to ECXb (ϕ = 13.3% in CH_2Cl_2), with excitation at 880 nm. The fluorescence quantum yield of ESi5 JV-aggregates in PBS (λ_{em} > 1000 nm) were referenced to IR26 (ϕ = 0.5% in 1,2-dichloroethane), with excitation at 980 nm. Specifically, the fluorescence quantum yield of the sample was calculated according to literature methods: Due to the fact that there still lacks a stable and bright dye absorbing in SWIR region with robustly calibrated fluorescence quantum yield, this quantum yield should be considered as an estimate.

Spectral deconvolution

Spectra deconvolution was conducted following literature methods (*J. Am. Chem. Soc*. 2022, **144**, 14351–14362).

Electron microscopy characterization

The stock solution containing **ESi5-S** or **ESi5-C1**(**-C5**) (5.0 mM, 40 μL) was prepared in methanol (MeOH) and then added to double-distilled water (960 μL) to induce aggregation. The resulting aggregate solution (0.2 mM) was incubated in the dark for 24 h, and the percentage of MeOH in the solution was diluted to 4%.

TEM samples were prepared by depositing 5 μL of aggregate solution on a 400-mesh formvar-supported copper grids coated with ultra-thin carbon film. After a 10-min deposition period, excess solution was removed using filter paper. The aggregate samples were imaged using JEM-1400 and JEM-2100 at an acceleration voltage of 100 kV.

Three microliters of solution containing aggregate was incubated on a mica sheet for 5 min and then was blotted with the filter paper until only a thin solution film remained. The AFM images were captured using a Bruker Dimension Fast Scan, using ScanAsyst mode under the ambient conditions.

For cryo-EM, the solution of aggregate (5 μL) was applied to glow-discharged holey carbon copper grids before plunge-frozen in liquid ethane after blotting with filter paper using Vitrobot Mark IV(FEI). Cryo-EM micrographs were acquired on a Tecnai T12 TEM (FEI), operated at an acceleration voltage of 120 kV.

Chemo-stability toward thiols and reactive oxygen species

An aliquot of GSH (0–10 mM) in H_2O, Cys (0–100 mM) in H_2O, NaSH (0–1 mM) in H_2O, H_2O_2 (0–10 mM) in H_2O, NaClO (0–50 μM) in H_2O (pH = 10), $ONOO^-$ (0–50 μM) in H_2O (pH = 10) were added into a solution of **ESi5-S agg**. The solution was stirred for 5 min before the absorption spectra were acquired.

Photostability tests

The **ESi5-S** monomer and **ICG** in DMSO with same absorbance (A = 0.2) in 808 nm were irradiated by an 808 nm laser (500 mW•cm^{-2}) with vigorous stirring for 30 min. The **ESi5-S agg** in PBS and **IR-1061** in DMSO with same absorbance (A = 0.2) in 1064 nm were irradiated by a 1064 nm laser (520 mW•cm^{-2}) with vigorous stirring for 30 min. The absorption of solutions was measured every 1 or 2 min.

The thermodynamic parameters for aggregation

The degree of aggregation and thermodynamic parameters for aggregation were calculated following literature methods (*Angew. Chem. Int. Ed*. 2012, **51**, 5615–5619).

In vitro hemolysis assay

Sheep red blood cells (2%, 0.5 mL) were incubated with Triton X-100 (2%, +), PBS buffer (pH = 7.4, 10 mM, −), and incremental concentration gradient of **ESi5-S agg** (20, 40, 60, 80, 100 μM) for 4 h on an oscillator at 37 °C, respectively. The suspension supernatant was concentrated by centrifugation (10,000 rpm, 5 min) and placed in a 96-well plate. The absorbance at 540 nm of each well was measured by enzyme marker, and the hemolytic percentage value was calculated according to Equation:

$$HP(\%) = \frac{OD_{Sample} - OD_{Saline}}{OD_{Triton} - OD_{Saline}} \times 100\%$$

Where OD_{sample}, OD_{saline}, and OD_{Triton} stand for the absorbance of sheep red blood cells incubated with different **ESi5-S agg**, PBS, and triton X-100, respectively.

In vivo dual-color fluorescence imaging by MARS system

Six to eight-week-old female BALB/c mice with a body weight of ~20 g were chosen for in vivo dual-color color fluorescence imaging. An aliquot of **ESi5-S agg** solution (500 μM in PBS, containing 4% DMSO, 100 μL) was injected into a BALB/c mouse through the tail vein to render a final vasculature concentration of 2.5 mg/kg, equivalent to a biocompatible blood concentration of *ca.* 30 μM. The whole-body images were acquired 10, 30, 60, 120, 180 min post injection. The images with excitation at 808 and 1064 nm were acquired sequentially. When the excitation of 808 nm (exposure time: 100 ms, 60 mW•cm^{-2}) was used, a long pass filter with a cutoff of 1200 nm was used for emission collection. When the excitation of 1064 nm (exposure time: 500 ms, 80 mW•cm^{-2}) was used, two long pass filters at 1350 and 1200 nm were used for emission collection. All mice were shaved before fluorescence imaging.

In vivo toxicity study

Six-week BALB/c female mouse ($n = 6$) was used as an animal model and randomly divided into three groups. An aliquot of PBS (10 mM, pH = 7.4, 0.1 mL) and **ESi5-S agg** (2.5 mg/kg, 5.0 mg/kg) solution was injected through the tail vein, respectively. The mice were raised for a period of 14 days, during which period the body weight and vitality of the mouse were recorded.

For H&E histology, the mice were sacrificed 24 h post *i.v.* injection of PBS (10 mM, pH = 7.4, 0.1 mL) and **ESi5-S agg** (2.47 mg/kg in PBS) and the major organs are harvested for H&E histology analysis for acute-toxicity features.

Photothermal conversion performance

The increase in temperature of **ESi5-S agg** solution (2 mL, in PBS) with different concentrations (0, 5, 10, 20, 30, 40, and 50 μM) under 1064 nm laser (1000 mW•cm^{-2}) and **ESi5-S agg** solution (30 μM in 2 mL PBS) under different power densities (200, 400, 600, 800, and 1000 mW•cm^{-2}) were measured using a temperature detector. The photothermal conversion efficiency (η) was calculated according to Equation:

$$\eta = \frac{hA(T_{\max} - T_{surr}) - Q_{dis}}{I(1 - 10^{-A1064})}$$

Where h is the heat transfer coefficient and A stands for the surface area of the quartz sample cell. $T_{\max}$ and T_{surr} are the maximum steady-state temperature under laser and the surrounding environment temperature, respectively. Q_{dis} is the heat dissipation from the light absorbed by the solvent and the quartz sample cell. I was the incident laser power, and A1064 represent the absorbance intensity of the solution at 1064 nm.

In vivo photoacoustic imaging

The photoacoustic signals of **ESi5-S agg** and IR-1061 solutions with different concentrations (0, 5, 10, 20, 30, 40, and 50 μM) were carried out with LOIS 3D (TomoWave Laboratories, USA) under 1064 nm laser.

For in vivo photoacoustic imaging, 6–8-week-old female BALB/c mice with a body weight of ~20 g ($n = 3$) were injected with **ESi5-S agg** (2.5 mg/kg, in PBS containing 4% DMSO). The PA imaging was performed by LOSI 3D imaging system before injected and post-injected of 120 min under 1064 nm laser. All mice were shaved before photoacoustic imaging.

Calcium-binding experiments

Hydroxyapatite (HA), calcium phosphate (CP), calcium pyrophosphate salts (CPP), calcium carbonate (CC), calcium oxalate (CO), and manganese dioxide (MnO_2) (10 mg/mL) were incubated separately with **ESi5-S agg** (10 μM) in PBS (pH = 7.4, 10 mM). The mixtures were vortexed for 60 min and then washed three times with PBS before centrifugated to remove unbound JV-aggregate. The precipitate was diluted in 200 μL PBS and the fluorescence emission intensity was tested.

Reporting summary

Further information on research design is available in the Nature Portfolio Reporting Summary linked to this article.

Data availability

Supplementary information is available. Requests for materials should be addressed to the corresponding author. The source data generated in this study have been deposited in the FigShare database under the accession code https://doi.org/10.6084/m9.figshare.27959742.v1. Source data are provided alongside the manuscript. Crystallographic data for the structures reported in this article have been deposited at the Cambridge Crystallographic Data Centre, under deposition numbers CCDC 2120399 (**ESi5•Cl**$^-$), and 2364282 (**ESi5•PF$_6^-$**). Copies of the data can be obtained free of charge via https://www.ccdc.cam.ac.uk/structures/. Data are available from the authors on request. Source data are provided with this paper.

References

1. Oliinyk, O. S. et al. Deep-tissue SWIR imaging using rationally designed small red-shifted near-infrared fluorescent protein. *Nat. Methods* **20**, 70–74 (2023).
2. Wang, F., Zhong, Y., Bruns, O., Liang, Y. & Dai, H. In vivo NIR-II fluorescence imaging for biology and medicine. *Nat. Photonics* **18**, 535–547 (2024).
3. Ibrahim, N. E.-S. Shortwave-infrared imaging of cancer vaccine uncovers immune response. *Nat. Rev. Bioeng.* **1**, 694–694 (2023).
4. Kantamneni, H. et al. Surveillance nanotechnology for multi-organ cancer metastases. *Nat. Biomed. Eng.* **1**, 993–1003 (2017).
5. Tang, X., Ackerman, M. M., Chen, M. & Guyot-Sionnest, P. Dual-band infrared imaging using stacked colloidal quantum dot photodiodes. *Nat. Photonics* **13**, 277–282 (2019).
6. Saran, R. & Curry, R. J. Lead sulphide nanocrystal photodetector technologies. *Nat. Photonics* **10**, 81–92 (2016).
7. Na, N. et al. Room temperature operation of germanium–silicon single-photon avalanche diode. *Nature* **627**, 295–300 (2024).
8. Baetens, R., Jelle, B. P. & Gustavsen, A. Properties, requirements and possibilities of smart windows for dynamic daylight and solar energy control in buildings: a state-of-the-art review. *Sol. Energy Mater. Sol. Cells* **94**, 87–105 (2010).
9. Wang, Z. Y. *Near-Infrared Organic Materials and Emerging Applications*. (CRC Press, 2013). https://doi.org/10.1201/b14775.
10. Tani, T., Suzumoto, T., Kemnitz, K. & Yoshihara, K. Picosecond kinetics of light-induced electron transfer from J-aggregated

cyanine dyes to silver bromide microcrystals: effect of aggregate size. *J. Phys. Chem.* **96**, 2778–2783 (1992).
11. Stuke, M. *Dye Lasers: 25 Years* Vol. 70 (Springer Berlin Heidelberg, 1992).
12. Xie, Y. et al. Bright short-wavelength infrared organic light-emitting devices. *Nat. Photonics* **16**, 752–761 (2022).
13. Liu, Y. et al. Versatile types of inorganic/organic NIR-IIa/IIb fluorophores: from strategic design toward molecular imaging and theranostics. *Chem. Rev.* **122**, 209–268 (2022).
14. Meador, W. E. et al. Silicon-RosIndolizine fluorophores with short-wave infrared absorption and emission profiles enable in vivo fluorescence imaging. *Nat. Chem.* **16**, 970–978 (2024).
15. Fukushima, H. et al. Cyanine phototruncation enables spatiotemporal cell labeling. *J. Am. Chem. Soc.* **144**, 11075–11080 (2022).
16. Nani, R. R., Kelley, J. A., Ivanic, J. & Schnermann, M. J. Reactive species involved in the regioselective photooxidation of heptamethine cyanines. *Chem. Sci.* **6**, 6556–6563 (2015).
17. Martin, A. & Rivera-Fuentes, P. A general strategy to develop fluorogenic polymethine dyes for bioimaging. *Nat. Chem.* **16**, 28–35 (2024).
18. Tolbert, L. M. & Ogle, M. E. How far can a carbanion delocalize? Carbon-13 NMR studies on soliton model compounds. *J. Am. Chem. Soc.* **112**, 9519–9527 (1990).
19. Brooker, L. G. S., Sprague, R. H., Smyth, C. P. & Lewis, G. L. Color and constitution. I. Halochromism of anhydronium bases related to the Cyanine Dyes1. *J. Am. Chem. Soc.* **62**, 1116–1125 (1940).
20. Tao, Z. et al. Biological imaging using nanoparticles of small organic molecules with fluorescence emission at wavelengths longer than 1000 nm. *Angew. Chem.* **125**, 13240–13244 (2013).
21. Antaris, A. L. et al. A high quantum yield molecule-protein complex fluorophore for near-infrared II imaging. *Nat. Commun.* **8**, 15269 (2017).
22. Lei, Y. et al. Supra-fluorophores: ultrabright fluorescent supramolecular assemblies derived from conventional fluorophores in water. *Adv. Mater.* **36**, 2401346 (2024).
23. Baumes, J. M. et al. Storable, thermally activated, near-infrared chemiluminescent dyes and dye-stained microparticles for optical imaging. *Nat. Chem.* **2**, 1025–1030 (2010).
24. Liu, W., Johnson, A. & Smith, B. D. Guest back-folding: a molecular design strategy that produces a deep-red fluorescent host/guest pair with picomolar affinity in water. *J. Am. Chem. Soc.* **140**, 3361–3370 (2018).
25. Li, D.-H., Schreiber, C. L. & Smith, B. D. Sterically shielded heptamethine cyanine dyes for bioconjugation and high performance near-infrared fluorescence imaging. *Angew. Chem. Int. Ed.* **59**, 12154–12161 (2020).
26. Li, D.-H. et al. Doubly strapped zwitterionic NIR-I and NIR-II heptamethine cyanine dyes for bioconjugation and fluorescence imaging. *Angew. Chem. Int. Ed.* **62**, e202305062 (2023).
27. Lei, Z. et al. Bright, stable, and biocompatible organic fluorophores absorbing/emitting in the deep near-infrared spectral region. *Angew. Chem. Int. Ed.* **56**, 2979–2983 (2017).
28. Li, J. et al. Stable, bright, and long-fluorescence-lifetime dyes for deep-near-infrared bioimaging. *J. Am. Chem. Soc.* **144**, 14351–14362 (2022).
29. Wei, R. et al. Rigid and photostable shortwave infrared dye absorbing/emitting beyond 1200 nm for high-contrast multiplexed imaging. *J. Am. Chem. Soc.* **145**, 12013–12022 (2023).
30. Kasha, M. Energy transfer mechanisms and the molecular exciton model for molecular aggregates. *Radiat. Res.* **20**, 55–70 (1963).
31. Nelson, N. & Ben-Shem, A. The complex architecture of oxygenic photosynthesis. *Nat. Rev. Mol. Cell Biol.* **5**, 971–982 (2004).
32. Hu, X. et al. J-aggregation strategy toward potentiated NIR-II fluorescence bioimaging of molecular fluorophores. *Adv. Mater.* **36**, 2304848 (2024).
33. Würthner, F., Kaiser, T. E. & Saha-Möller, C. R. J-aggregates: from serendipitous discovery to supramolecular engineering of functional dye materials. *Angew. Chem. Int. Ed.* **50**, 3376–3410 (2011).
34. Mei, J., Leung, N. L. C., Kwok, R. T. K., Lam, J. W. Y. & Tang, B. Z. Aggregation-induced emission: together we shine, united we soar! *Chem. Rev.* **115**, 11718–11940 (2015).
35. Tian, Y., Yin, D. & Yan, L. J-aggregation strategy of organic dyes for near-infrared bioimaging and fluorescent image-guided phototherapy. *WIREs Nanomed. Nanobiotechnol.* **15**, e1831 (2023).
36. Kobayashi, T. *J-Aggregates* Vol. 2. (World Scientific, 2012).
37. Hannah, K. C. & Armitage, B. A. DNA-templated assembly of helical cyanine dye aggregates: a supramolecular chain polymerization. *Acc. Chem. Res.* **37**, 845–853 (2004).
38. Li, K. et al. J-aggregates of meso-[2.2]paracyclophanyl-BODIPY dye for NIR-II imaging. *Nat. Commun.* **12**, 2376 (2021).
39. Chen, W. et al. Shortwave infrared imaging with j-aggregates stabilized in hollow mesoporous silica nanoparticles. *J. Am. Chem. Soc.* **141**, 12475–12480 (2019).
40. Grande, V., Soberats, B., Herbst, S., Stepanenko, V. & Würthner, F. Hydrogen-bonded perylene bisimide J-aggregate aqua material. *Chem. Sci.* **9**, 6904–6911 (2018).
41. Huynh, E. et al. In situ conversion of porphyrin microbubbles to nanoparticles for multimodality imaging. *Nat. Nanotechnol.* **10**, 325–332 (2015).
42. Sun, C. et al. J-aggregates of cyanine dye for NIR-II in vivo dynamic vascular imaging beyond 1500 nm. *J. Am. Chem. Soc.* **141**, 19221–19225 (2019).
43. Chen, Z. et al. Near-IR absorbing J-aggregate of an amphiphilic BF2-azadipyrromethene dye by kinetic cooperative self-assembly. *Angew. Chem. Int. Ed.* **56**, 5729–5733 (2017).
44. Draper, E. R. et al. pH-directed aggregation to control photoconductivity in self-assembled perylene bisimides. *Chem* **2**, 716–731 (2017).
45. Kim, J. H. et al. An efficient narrowband near-infrared at 1040 nm organic photodetector realized by intermolecular charge transfer mediated coupling based on a squaraine dye. *Adv. Mater.* **33**, 2100582 (2021).
46. Ma, X. et al. J-aggregates formed by NaCl treatment of aza-coating heptamethine cyanines and their application to monitoring salt stress of plants and promoting photothermal therapy of tumors. *Angew. Chem. Int. Ed.* **62**, e202216109 (2023).
47. Lovell, J. F. et al. Porphysome nanovesicles generated by porphyrin bilayers for use as multimodal biophotonic contrast agents. *Nat. Mater.* **10**, 324–332 (2011).
48. Wei, K. et al. A light-triggered J-aggregation-regulated therapy conversion: from photodynamic/photothermal therapy to long-lasting chemodynamic therapy for effective tumor ablation. *Angew. Chem. Int. Ed.* **63**, e202404395 (2024).
49. Cai, K. et al. Concurrent cooperative J-aggregates and anticooperative H-aggregates. *J. Am. Chem. Soc.* **140**, 5764–5773 (2018).
50. Herbst, S. et al. Self-assembly of multi-stranded perylene dye J-aggregates in columnar liquid-crystalline phases. *Nat. Commun.* **9**, 2646 (2018).
51. Zhang, Q. et al. Bright and stable NIR-II J-aggregated AIE dibodipy-based fluorescent probe for dynamic in vivo bioimaging. *Angew. Chem. Int. Ed.* **60**, 3967–3973 (2021).
52. Guo, X. et al. Tuning shortwave-infrared J-aggregates of aromatic ring-fused aza-BODIPYs by peripheral substituents for combined photothermal and photodynamic therapies at ultralow laser power. *Angew. Chem.* **136**, e202319875 (2024).
53. Freytag, E. et al. Chiroptical properties of planar benzobisthiazole-bridged squaraine dimers. *J. Org. Chem.* **88**, 10777–10788 (2023).
54. Shen, C.-A., Stolte, M., Kim, J. H., Rausch, A. & Würthner, F. Double J-coupling strategy for near infrared emitters. *J. Am. Chem. Soc.* **143**, 11946–11950 (2021).

55. Eisele, D. M. et al. Utilizing redox-chemistry to elucidate the nature of exciton transitions in supramolecular dye nanotubes. *Nat. Chem.* **4**, 655–662 (2012).
56. Hou, T.-C., Wu, Y.-Y., Chiang, P.-Y. & Tan, K.-T. Near-infrared fluorescence activation probes based on disassembly-induced emission cyanine dye. *Chem. Sci.* **6**, 4643–4649 (2015).
57. Bricks, J. L., Slominskii, Y. L., Panas, I. D. & Demchenko, A. P. Fluorescent J-aggregates of cyanine dyes: basic research and applications review. *Methods Appl. Fluoresc.* **6**, 012001 (2017).
58. Feng, L. et al. A facile structural isomerization-induced 3D spatial D-A interlocked network for achieving NIR-II phototheranostic agents. *Angew. Chem. Int. Ed.* **61**, e202212673 (2022).
59. Lee, K.-W. et al. Anti-quenching NIR-II J-aggregates of benzo[c] thiophene fluorophore for highly efficient bioimaging and phototheranostics. *Adv. Mater.* **35**, 2211632 (2023).
60. Kaiser, T. E., Wang, H., Stepanenko, V. & Würthner, F. Supramolecular construction of fluorescent J-aggregates based on hydrogen-bonded perylene dyes. *Angew. Chem. Int. Ed.* **46**, 5541–5544 (2007).
61. Deshmukh, A. P. et al. Near-atomic-resolution structure of J-aggregated helical light-harvesting nanotubes. *Nat. Chem.* **16**, 800–808 (2024).
62. Bailey, A. D. et al. Exploring the design of superradiant J-aggregates from amphiphilic monomer units. *Nanoscale* **15**, 3841–3849 (2023).
63. Eisele, D. M., Knoester, J., Kirstein, S., Rabe, J. P. & Vanden Bout, D. A. Uniform exciton fluorescence from individual molecular nanotubes immobilized on solid substrates. *Nat. Nanotechnol.* **4**, 658–663 (2009).
64. Hestand, N. J. & Spano, F. C. Expanded theory of H- and J-molecular aggregates: the effects of vibronic coupling and intermolecular charge transfer. *Chem. Rev.* **118**, 7069–7163 (2018).
65. Shi, Y. et al. Small energetic disorder enables ultralow energy losses in non-fullerene organic solar cells. *Adv. Energy Mater.* **13**, 2300458 (2023).
66. Han, G. & Yi, Y. Molecular insight into efficient charge generation in low-driving-force nonfullerene organic solar cells. *Acc. Chem. Res.* **55**, 869–877 (2022).
67. Tkacheva, T. N., Yefimova, S. L., Klochkov, V. K., Borovoy, I. A. & Malyukin, Y. V. Spectroscopic study of ordered hybrid complexes formation between dye aggregates and ReVO4:Eu3 + (Re = Y, Gd, La) nanoparticles. *J. Mol. Liq.* **199**, 244–250 (2014).
68. Wang, H. et al. P800SO3-PEG: a renal clearable bone-targeted fluorophore for theranostic imaging. *Biomater. Res.* **26**, 51 (2022).

Acknowledgements

This work was supported by the National Key Research and Development Program of China (no. 2022YFD1700800), the National Natural Science Foundation of China (nos. 22078098 and 22278138), the Fundamental Research Funds for the Central Universities, the Shanghai Academic/Technology Research Leader (22XD1421000), the Open Funding Project of the State Key Laboratory of Bioreactor Engineering, and the State Key Laboratory of Fine Chemicals (KF2202). The authors thank Qi Zhang, Weiping Zhu, and Haibo Yang for insightful discussions.

Author contributions

C.Y. was responsible for synthesis, spectral studies, draft preparation, and editing. R.W., X.Z., and R.C. contributed to the synthesis. J.Z. and J.C. carried out transient absorption studies. Y.S. and J.R. contributed to TEM. W.X. and C.L. contributed to cryo-EM studies. D.Q. contributed to the vary-temperature experiment. Y.W. contributed to AFM studies. X.L. Y.D., and G.G. contributed to in vivo imaging. X.L. and X.Q. were responsible for advising and editing. Y.Y was responsible for advising, editing, and conceptualization.

Competing interests

A Chinese patent application (2024115961715) with Y.Y., X.Q., X.L., and C.Y. listed as inventors is filed for the structures, preparation, and potential applications of the aggregates described in this manuscript. Y.Y., X.Q., X.L., and C.Y. declare no other competing interests. Other authors declare no competing interests.

Additional information

Supplementary information The online version contains supplementary material available at https://doi.org/10.1038/s41467-024-55445-x.

Correspondence and requests for materials should be addressed to Youjun Yang.

Peer review information *Nature Communications* thanks the anonymous reviewers for their contribution to the peer review of this work. A peer review file is available.